

Retraction

Retracted: Three-Dimensional Inversion of Borehole-Surface Resistivity Method Based on the Unstructured Finite Element

International Journal of Antennas and Propagation

Received 19 December 2023; Accepted 19 December 2023; Published 20 December 2023

Copyright © 2023 International Journal of Antennas and Propagation. This is an open access article distributed under the Creative Commons Attribution License, which permits unrestricted use, distribution, and reproduction in any medium, provided the original work is properly cited.

This article has been retracted by Hindawi following an investigation undertaken by the publisher [1]. This investigation has uncovered evidence of one or more of the following indicators of systematic manipulation of the publication process:

- (1) Discrepancies in scope
- (2) Discrepancies in the description of the research reported
- (3) Discrepancies between the availability of data and the research described
- (4) Inappropriate citations
- (5) Incoherent, meaningless and/or irrelevant content included in the article
- (6) Manipulated or compromised peer review

The presence of these indicators undermines our confidence in the integrity of the article's content and we cannot, therefore, vouch for its reliability. Please note that this notice is intended solely to alert readers that the content of this article is unreliable. We have not investigated whether authors were aware of or involved in the systematic manipulation of the publication process.

Wiley and Hindawi regrets that the usual quality checks did not identify these issues before publication and have since put additional measures in place to safeguard research integrity.

We wish to credit our own Research Integrity and Research Publishing teams and anonymous and named external researchers and research integrity experts for contributing to this investigation.

The corresponding author, as the representative of all authors, has been given the opportunity to register their agreement or disagreement to this retraction. We have kept a record of any response received.

References

- [1] Z. Wang and S. Fang, "Three-Dimensional Inversion of Borehole-Surface Resistivity Method Based on the Unstructured Finite Element," *International Journal of Antennas and Propagation*, vol. 2021, Article ID 5154985, 13 pages, 2021.

Research Article

Three-Dimensional Inversion of Borehole-Surface Resistivity Method Based on the Unstructured Finite Element

Zhi Wang¹ and Sinan Fang²

¹Electronics and Information School, Yangtze University, Jingzhou 434023, China

²College of Geophysics and Petroleum Resources, Yangtze University, Wuhan 430100, China

Correspondence should be addressed to Zhi Wang; 1324385898@qq.com

Received 11 August 2021; Revised 25 August 2021; Accepted 12 September 2021; Published 24 September 2021

Academic Editor: Jin He

Copyright © 2021 Zhi Wang and Sinan Fang. This is an open access article distributed under the Creative Commons Attribution License, which permits unrestricted use, distribution, and reproduction in any medium, provided the original work is properly cited.

The electromagnetic wave signal from the electromagnetic field source generates induction signals after reaching the target geological body through the underground medium. The time and spatial distribution rules of the artificial or the natural electromagnetic fields are obtained for the exploration of mineral resources of the subsurface and determining the geological structure of the subsurface to solve the geological problems. The goal of electromagnetic data processing is to suppress the noise and improve the signal-to-noise ratio and the inversion of resistivity data. Inversion has always been the focus of research in the field of electromagnetic methods. In this paper, the three-dimensional borehole-surface resistivity method is explored based on the principle of geometric sounding, and the three-dimensional inversion algorithm of the borehole-surface resistivity method in arbitrary surface topography is proposed. The forward simulation and calculation start from the partial differential equation and the boundary conditions of the total potential of the three-dimensional point current source field are satisfied. Then the unstructured tetrahedral grids are used to discretely subdivide the calculation area that can well fit the complex structure of subsurface and undulating surface topography. The accuracy of the numerical solution is low due to the rapid attenuation of the electric field at the point current source and the nearby positions and sharply varying potential gradients. Therefore, the mesh density is defined at the local area, that is, the vicinity of the source electrode and the measuring electrode. The mesh refinement can effectively reduce the influence of the source point and its vicinity and improve the accuracy of the numerical solution. The stiffness matrix is stored with Compressed Row Storage (CSR) format, and the final large linear equations are solved using the Super Symmetric Over Relaxation Preconditioned Conjugate Gradient (SSOR-PCG) method. The quasi-Newton method with limited memory (L_BFGS) is used to optimize the objective function in the inversion calculation, and a double-loop recursive method is used to solve the normal equation obtained at each iteration in order to avoid computing and storing the sensitivity matrix explicitly and reduce the amount of calculation. The comprehensive application of the above methods makes the 3D inversion algorithm efficient, accurate, and stable. The three-dimensional inversion test is performed on the synthetic data of multiple theoretical geoelectric models with topography (a single anomaly model under valley and a single anomaly model under mountain) to verify the effectiveness of the proposed algorithm.

1. Introduction

Owing to the need for energy development and the development of remote sensing technology, the research of electromagnetic wave propagation and its application in communication and detection has made significant progress. It has been used in radio communications in mine tunnels, railway tunnels, and military tunnels; communications with

submarines, command, and navigation; and the electromagnetic wave detection of mineral resources and crustal structures [1, 2] (including faults, glaciers, caves, pipelines, water sources, and objects in the ocean). The wave-field structure is an important problem for communication and detection systems [3–9]. Electromagnetic exploration is based on the electrical differences between different rocks in the Earth's crust (such as differences in electrical conductivity,

magnetic permeability, dielectric, and electrochemical properties). The electromagnetic field signal sent by the field source passes through the underground medium to reach the target geological body and then generates an induction signal. These electromagnetic waves containing the induction signal of the target geological body are received by the receiver arranged in the well or on the ground. In this paper, the influence of geometric and electromagnetic characteristics of various geological structures (including man-made structures) on electromagnetic wave propagation is studied. The time and space distributions of artificial or natural electromagnetic fields are observed and analyzed to determine useful underground mineral resources, identify underground geological structures, and solve the geological problems [1]. Electromagnetic exploration methods are mainly divided into direct current method based on the principle of geometric sounding, magnetotelluric method (MT/AMT/CSAMT) based on the principle of frequency domain sounding, and transient electromagnetic method (TEM) based on the principle of time-domain sounding [2]. The direct current (DC) resistivity method is one of the classic methods of geoelectric exploration. It has been widely and effectively applied in mineral resources (metallic and nonmetallic minerals, coal fields, oil, and gas), environmental engineering (groundwater, geological landslides, and environmental monitoring), geotechnical engineering (tunnel construction and mine water inrush), and other fields. Moreover, the DC resistivity method has been expanded to hydrology, archaeology, and other fields that are closely related to national economic construction and human social life. The DC resistivity method has a variety of flexible observation methods such as the electrical profile method and electrical sounding method with different electrode arrays, pole-pole, dipole-dipole, and multipole. The high-density electrical method has been introduced, which can efficiently obtain large observation data, making it possible for the three-dimensional resistivity inversion of underground fine structures [10]. The borehole-surface resistivity method is a type of electrical method in which electrodes are placed in the well and on the ground. The electrode in the well is the source electrode and the electrode on the ground receiving the electromagnetic field is measured. The source electrode is always placed in the deep part of the borehole to make it close to the object to be detected, thereby increasing the current intensity or the received abnormal response [11]. The borehole-surface resistivity method is mainly used for secondary resource exploration in metal mines and the prediction of oil reservoir boundaries [12]. Data are collected on a grid along parallel lines with different electrode arrays, and a 3D inversion algorithm is used. With the development of computer and numerical computing technology, the three-dimensional electromagnetic forward and inversion algorithms have made significant progress in the mesh design (structured [13–16] and unstructured [17–25]), as well as the numerical method in the forward solution (finite difference [26–30] and finite element [31, 32]), solving the objective function (Gauss–Newton (GN) method [33–37], quasi-Newton (QN) method [38–50], nonlinear conjugate gradient (NLCG) method [51–53], etc.).

The unstructured finite element method (FEM) has achieved promising success in the three-dimensional numerical simulation of resistivity in complex topography. The unstructured grid allows local densification and can simulate complex geometric models. The structure also has controllable element quality and its solution efficiency significantly increases in the three-dimensional unstructured FEM. The calculation time and the storage capacity of the unstructured grid can be reduced by about an order of magnitude retaining the same calculation accuracy as the structured grid [10]. Owing to a large number of inversion parameters and a vast amount of data in the three-dimensional resistivity inversion, the Jacobian matrix (partial derivative matrix) has huge calculation and storage requirements. Many inversion algorithms have been proposed which can avoid the calculation of the Jacobian matrix. Zhang et al. [26] and Wu and Xu [54] introduced the conjugate gradient method to achieve fast and effective three-dimensional resistivity inversion and resolve the issues of solution and storage of the Jacobian matrix in the three-dimensional inversion to improve the efficiency. The optimization methods used in 3D data inversion mainly include the nonlinear conjugate gradient (NLCG) method, the Gauss-Newton (GN) method, and the quasi-Newton (QN) method. Both the NLCG and the QN only need the gradient information of the objective function, and no explicit sensitivity matrix is needed. The GN method has second-order sensitivity information, and the inversion convergence speed is better but the calculation speed is lower than that of the QN and the NLCG methods. The QN method approximately computes the inverse Hessian matrix in the iterative process and is more efficient than the NLCG method in the step size search. In the large-scale 3D data inversion, the QN method still has the problem of occupying memory. Therefore, the limited memory quasi-Newton method (L_BFGS) has been developed. The L_BFGS method only needs to store the last m iterations information to generate the inverse Hessian matrix, which significantly reduces the required memory. With the expansion of the application range of the DC resistivity method, the study of inversion accuracy and inversion speed in the 3D resistivity inversion method has important practical significance and theoretical value.

In the above-mentioned studies, the L_BFGS method has the advantages of fast convergence, less memory, and better inversion efficiency than the other inversion algorithms. The L_BFGS is also more suitable for solving large-scale 3D electromagnetic inversion problems. Therefore, an inversion algorithm for the three-dimensional resistivity method with the undulating terrain is developed in this paper by combining the L_BFGS method, the borehole-to-surface observation method, and the FEM with unstructured tetrahedrons. Numerical results of the theoretical model inversion validate the effectiveness of the proposed method.

2. Forward Modeling Theory

2.1. Base Equation. The partial differential equation and its boundary-value problem satisfied by the total potential of the three-dimensional point current source field are given by the following equation with mixed boundary conditions [14, 55]:

$$\begin{aligned} \nabla \cdot (\sigma(x, y, z) \nabla u(x, y, z)) &= -\frac{4\pi}{\omega_A} I \delta(\mathbf{r}_A), \quad \text{in } \Omega, \\ \frac{\partial u}{\partial \mathbf{n}} &= 0, \quad \text{on } \Gamma_s, \\ \frac{\partial u}{\partial \mathbf{n}} + \frac{\cos \theta}{r} u &= 0, \quad \text{on } \Gamma_\infty, \end{aligned} \quad (1)$$

where σ is the conductivity distribution on the surface, \mathbf{u} is the electrical potential, I is the strength of the source, δ is the Dirac delta function, \mathbf{r}_A is the coordinate of the source electrode A , ω_A is the opening angle of the source to the underground Earth by Ω , \mathbf{n} is the outward normal to the boundary surface Γ_∞ of the modal domain, r is the location of an arbitrary potential electrode from the source point, Γ_s and Γ_∞ are the natural boundary condition (surface-air interface) and the infinite boundary condition (artificially cut off the interface), respectively, and θ is the angle between the radial distance \mathbf{r} from the source point and the outward normal spatial coordinate n on the boundary. If the source point is on the ground, then $\omega_A = 2\pi$, while if the source point is underground, then $\omega_A = 4\pi$. The weighted residual method can be used to derive the integral equation of the variational problem corresponding to equation (1) [15, 55]:

$$\begin{aligned} F(u) &= \int_{\Omega} \left[\frac{1}{2} \sigma (\nabla u)^2 - \frac{4\pi}{\omega_A} \delta(A) u \right] d\Omega \\ &+ \int_{\Gamma_\infty} \frac{1}{2} \sigma u^2 \frac{\cos(\mathbf{r}, \mathbf{n})}{r} d\Gamma, \quad (2) \\ \delta F(u) &= 0. \end{aligned}$$

The calculation area adopts tetrahedral division and linear difference and finally forms a large sparse symmetric linear equation system. The matrix expression is as follows:

$$\mathbf{K}\mathbf{u} = \mathbf{P}, \quad (3)$$

where \mathbf{K} is an $n \times n$ symmetric matrix, \mathbf{u} is an $n \times 1$ column vector representing the potential vector on the three-dimensional grid node, and \mathbf{P} is a column vector containing field source information. In order to save memory, the Compressed Sparse Row or Compressed Row Storage is used to store the coefficient matrix \mathbf{K} , and the Super Symmetric Over Relaxation Preconditioned Conjugate Gradient (SSOR-PCG) algorithm [16, 25] is used to solve equation (3).

2.2. Algorithm Verification. In order to verify the correctness of the proposed algorithm, a buried spherical model in a uniform half-space is selected. All calculations in this article are done on a computer consisting of an Intel i7-4712 MQ CPU with a frequency of 2.3 GHz and 16 G memory. Both forward and inversion programs are compiled and run by Intel Fortran. Gmsh 4.8.4 [56] and ParaView 5.6.0 [57] are used for generating and visualizing the unstructured tetrahedral meshes, respectively.

Figure 1 shows the model for the spherical anomaly embedded in a uniform half-space (Ren and Tang [20]). The

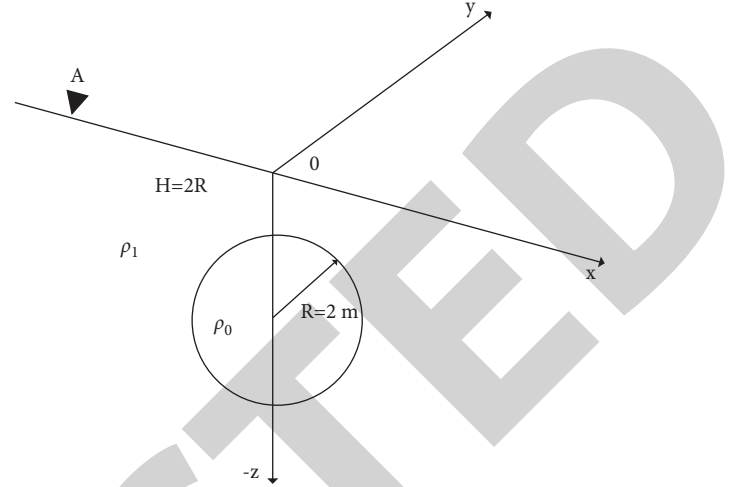


FIGURE 1: The geometric structure of the sphere model.

radius, the center coordinates, and the resistivity of the sphere are $R=2.25$ m, $(0, 0, -4.5)$, and $\rho_0 = 1 \Omega\text{m}$, respectively, the resistivity of the half-space is $\rho_1 = 10 \Omega\text{m}$, the point current source electrode A is at $(-5, 0, 0)$, and a current source of strength 1A is injected into the Earth. The measuring electrodes M are along the X direction with spacing of 0.25 m. The spatiality of the entire calculation area is $500 \text{ m} \times 500 \text{ m} \times 500 \text{ m}$.

The target area size is $100 \text{ m} \times 100 \text{ m} \times 100 \text{ m}$. The meshes at the source and the measurement points are refined, the total number of grid nodes is 56737, and the total number of grid cells is 277375. Figure 2 shows the partial magnification effect of the mesh division. The source point, the measuring point, and the anomalous body were refined meshes. The potential value at the measuring point is calculated by the finite element forward modeling program in this article with the pole-pole device and compared with the analytical solution given by Cook and Van Nostrand [58]. Figure 3 compares the analytical and numerical solutions of apparent resistivity of an underground spheroid. Figure 4 presents the relative error of the analytical and numerical solutions of apparent resistivity in the sphere model. It can be seen from Figure 4 that the maximum error is less than 1.4%.

3. Inversion Theory

3.1. Objective Function. According to Tikhonov's regularization theory, the inversion objective function in the sense of least squares is used. The objective function is described as [10, 18]

$$\begin{aligned} \Phi(m) &= \Phi_d(\mathbf{m}) + \lambda \Phi_m(\mathbf{m}) = \|\mathbf{W}_d(\mathbf{d}_{\text{obs}} - F(\mathbf{m}))\|_2^2 \\ &+ \lambda \|\mathbf{W}_m(\mathbf{m} - \mathbf{m}_{\text{ref}})\|_2^2, \quad (4) \end{aligned}$$

where $F(\mathbf{m})$ is the forward response function, m is the model parameter ($m_i, i = 1, 2, \dots, M$), \mathbf{d}_{obs} is the observation data, \mathbf{W}_d is an $N \times N$ data weighting matrix (N is the number of data) in which the diagonal elements are the measured data

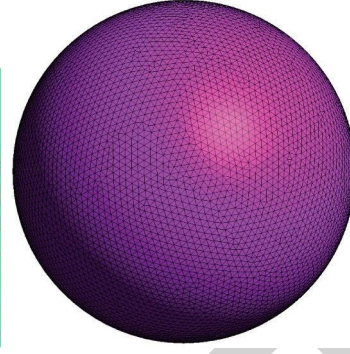
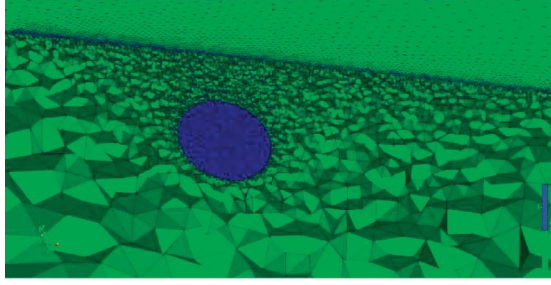


FIGURE 2: Partial magnification effect of the mesh division.

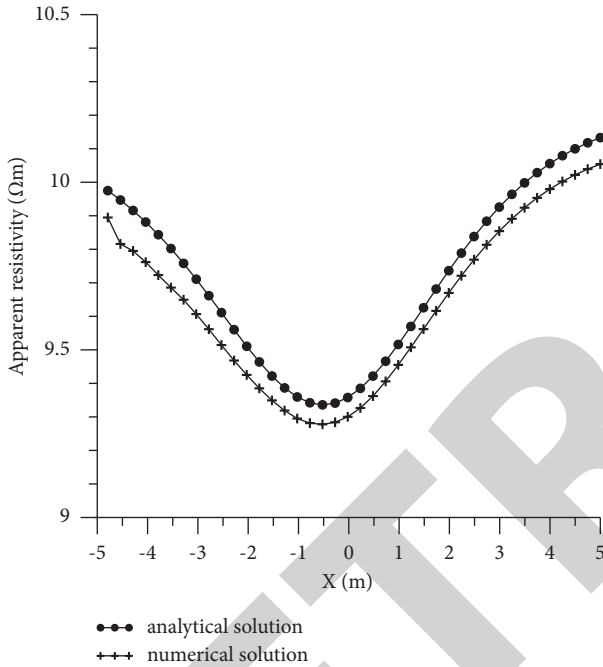


FIGURE 3: Comparison of analytical and numerical solutions of apparent resistivity of the underground spheroid.

and the remaining elements are zero, σ_i is the standard deviation of the i -th measured data, \mathbf{W}_m is the model-weighted matrix usually defined by the discrete difference operator of the model unit and generally takes the first-order regularization constraint, λ is the regularization parameter used to balance the weight of data fitting and model smoothness, and \mathbf{m}_{ref} is a reference model containing prior information about the model parameters. The inverted measured data \mathbf{d}_{obs} are the pole-pole potential value and the model parameter is the conductivity value of the element. Usually, the logarithm is used to calibrate the measured data and the model parameters mainly due to the large variation range and to invert the stability. The logarithm is defined as $d = \ln \phi_{\text{obs}}$, $m = \ln \sigma$. The resistivity inversion problem is generally a mixed problem, which often leads to equation (4) as an ill-conditioned equation. To solve this problem, smooth constraints are introduced into the inversion equation. Unstructured grid with disorderly arrangement was used in the forward modeling, so we adopt smooth constraint

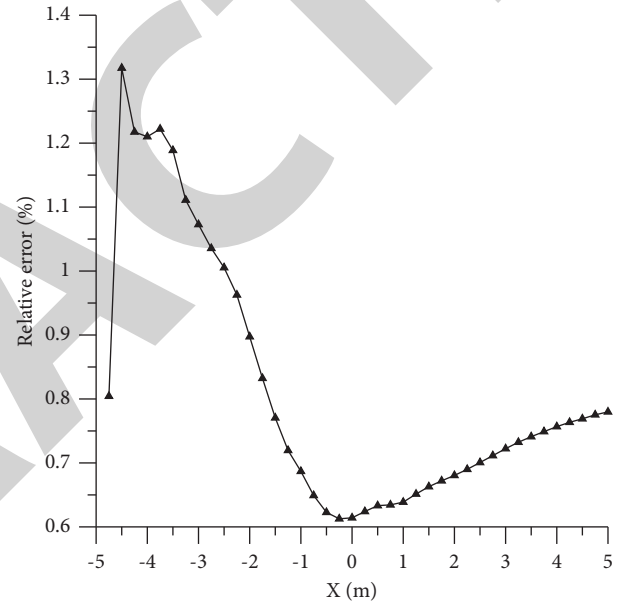


FIGURE 4: Relative error.

method, that is, judge the adjacency of the grid according to whether the grid unit has contact surface to determine the adjacency of the grid unit. For adjacency to generate matrix \mathbf{W}_m , $W_m(i, j)$ represents the contribution of the j -th unit to the smoothness of the i -th unit, which is generated according to the following formula:

$$W_m = \begin{cases} \frac{(1/x_{ij})}{\sum_{j=1}^{k_i} (1/x_{ij})}, & i \text{ and } j \text{ are adjacent units,} \\ 1, & i = j, \\ 0, & \text{other,} \end{cases} \quad (5)$$

where $x_{ij} = |x_i - x_j|$, and it is the distance in the X direction between the center of the i -th unit and the j -th unit, and k_i is the number of adjacent units to the i -th unit.

3.2. *Inversion Framework.* For the large-scale inversion problem, the traditional BFGS method requires a large

amount of memory. Nocedal [50] improved the BFGS method and proposed a limited memory BFGS (L_BFGS) method to solve the nonlinear optimization problem. In the

L_BFGS method, the inverse Hessian matrix approximation formula is defined as

$$\begin{aligned}
\mathbf{H}_{k+1} &= (V_{k-1}^T, \dots, V_{k-m}^T) \mathbf{H}_k^0 (V_{k-m}, \dots, V_{k-1}) \\
&+ \rho_{k-m} (V_{k-1}^T, \dots, V_{k-m+1}^T) s_{k-m} s_{k-m}^T (V_{k-m+1}, \dots, V_{k-1}) \\
&+ \rho_{k-m+1} (V_{k-1}^T, \dots, V_{k-m+2}^T) s_{k-m+1} s_{k-m+1}^T (V_{k-m+2}, \dots, V_{k-1}) + \dots + \rho_{k-1} s_{k-1} s_{k-1}^T, \\
\rho_k &= \frac{1}{y_k^T s_k}, \\
V_k &= (I - \rho_k y_k s_k^T), \\
s_k &= m_{k+1} - m_k, \\
y_k &= g_{k+1} - g_k,
\end{aligned} \tag{6}$$

where m is the number of previous iterations with a value between 3 and 20. The previous iteration information of gradient and the model modification is used to modify the inverse Hessian matrix. \mathbf{H}_k^0 defined by Nocedal and Wright [59] gives an update method as

$$\mathbf{H}_k^0 = \gamma_k \mathbf{I}. \tag{7}$$

In this paper, the identity matrix I is selected to initialize matrix \mathbf{H}_k^0 and γ_k can be defined as

$$\gamma_k = \frac{s_{k-1}^T y_{k-1}}{y_{k-1}^T y_{k-1}}. \tag{8}$$

The inversion steps of the L_BFGS method are defined in Algorithm 1 as follows [49, 59].

In the algorithm, g_k is the gradient of the objective function (4), and it is expressed as

$$g_k = \nabla \Phi(m_k) = -2J_m^T W_d^T W_d (d_{\text{obs}} - F(m_k)) + 2\lambda W_m^T W_m m_k, \tag{9}$$

where J represents the Jacobian matrix. It can be seen from formula (9) that the calculation of the gradient lies in the calculation of the Jacobian matrix. The explicit calculation requires massive computation and memory storage. Therefore, it is necessary to avoid directly calculating the Jacobian matrix and calculate the product of the transpose of the Jacobian matrix and any one-dimensional vector. Thus, there is no need for storing the Jacobian matrix, and the calculation can be obtained together after the forwarding in each inversion, which significantly speeds up the inversion calculation. The calculation details are provided by Zhanget al. [26].

Nocedal and Wright [59] presented a double-loop recursive method to update Step 2 in Algorithm 1. The detailed calculation process can be found in the literature [59]. In the process of minimizing the objective function, in contrast to

the CG's method in which the step size is obtained using an analytical method, both the NLCG and the L_BFGS methods need to obtain the iterative step size through an inexact one-dimensional linear search method. In this article, the iterative step size is required to meet the sufficient descent condition and the curvature condition. The Wolfe-Powell criterion can be obtained as

$$\Phi(m_k + \alpha_k p_k) \leq \Phi(m_k) + c_1 \alpha_k \nabla \Phi(m_k)^T p_k, \tag{10}$$

$$\nabla \Phi(m_k + \alpha_k p_k)^T p_k \geq c_2 \nabla \Phi(m_k)^T p_k,$$

where Φ is the forward operator, m_k is the model parameter of the k -th inversion iteration, α_k is the iteration step length, c_1 and c_2 are constants satisfying $0 < c_1 < c_2 < 1$, and p_k is the search direction. The search methods product can be calculated using the process described in the work of Nocedal and Wright [59]. In general, the smaller c_2 is, the more accurate the linear search will be. If $c_2 = 0.1$, a fairly accurate linear search will be obtained, while $c_2 = 0.9$ will result in a relatively weak linear search. The smaller c_2 , the longer the search time. According to the literature, the commonly used values c_1 and c_2 in the L_BFGS method are $c_1 = 10^{-4}$ and $c_2 = 0.9$.

4. Synthetic Data Inversion

In actual exploration, the influence of topography is unavoidable and will cause deviations in the inversion results. Topography correction is usually used to eliminate the impact. However, since the underground structure is complex, the topography correction can only be approximated and will still have large errors. Therefore, regardless of the topography correction in the data or the model space, the resistivity inversion under undulating topography conditions cannot eliminate the influence of the terrain. The influence of the topography can be accurately eliminated

- (1) Set $k = 1$, choose initial model \mathbf{m}_0 , integer $m > 0$ and initial matrix \mathbf{H}_k^0 (the identity matrix);
- (2) Compute $p_k = -H_k g_k$, $m_{k+1} = m_k + \alpha_k p_k$, where α_k is selected to satisfy the Wolfe-Powell conditions;
- (3) If $k > m$ then
 - Discard the vector pair $\{s_{k-m}, y_{k-m}\}$ from the storage
 - Compute and save $s_k = m_{k+1} - m_k$, $y_k = g_{k+1} - g_k$;
 end
- (4) Update \mathbf{H}_k^0 using formula (7) for m times to obtain \mathbf{H}_{k+1} from formula (6);
- (5) Set $k = k + 1$, go to step 2.

ALGORITHM 1: Limited Memory BFGS.

only by incorporating the topography into the inversion algorithm [10]. In this paper, the topography information is directly introduced in the inversion and the three-dimensional resistivity inversion with topography is conducted. Numerical examples over different scenarios are provided to illustrate the validity of the inversion algorithm proposed in this paper. A single low-resistance anomaly model is embedded with measured data for three-dimensional inversion under the flat, valley, and mountain topographies.

4.1. Inversion of Buried Cuboid Model under Flat Topography.

The rectangular model is shown in Figure 5. The resistivities of the background half-space and the low-resistance body are $\rho_0 = 100 \Omega\text{m}$ and $\rho_1 = 10 \Omega\text{m}$, respectively. The size of the low-resistance cuboid is $10 \text{ m} \times 10 \text{ m} \times 5 \text{ m}$. The buried depths of the cuboid from the top to the ground and from the bottom to the ground are $h = 5 \text{ m}$ and 10 m , respectively. The blue triangles represent the locations of the two well-heads $(40, 50, 0)$ and $(60, 50, 0)$. The red five-pointed star represents the origin of the Cartesian coordinate system $(50, 50, 0)$, and the horizontal distance between the anomalous body and the drilling on both sides is $d = 5 \text{ m}$. The survey line range used in inversion is $1 \sim 99 \text{ m}$ and the spacing between survey lines is 1 m . The number of selected measuring points in each survey line is 99, and the position coordinates of measuring point M (measuring electrode) along the X direction are $x = 1 \sim 99 \text{ m}$ and $y = 1 \sim 99 \text{ m}$, while the spacing is 1 m . The range of the source point A (source electrode) is from -5 m to -25 m downhole, with an interval of 5 m . Figures 6(a) and 6(b) are the unstructured tetrahedral grids used in forward modeling and inversion, respectively. In order to improve the accuracy of forward modeling and reduce the numerical simulation errors near the source point, the forward modeling grids are measured, the source point and the vicinity of the anomalous body are refined meshes, and the total number of tetrahedra grids is 1706788. The inversion grid is refined at the source and the measurement points, and the total number of tetrahedra grids is 1512967. A total of 98,010 pieces of "potential measured data" of the primary field were obtained by using a pole-pole array and the three-dimensional finite element forward modeling program. In order to verify the stability of the proposed inversion algorithm, 3% Gaussian noise was added to the theoretical measured data. The selection of the inversion parameters is as follows: the regularization parameter $\lambda = 0.05$, which remains unchanged during the

inversion process, the convergence coefficient of the inversion termination, and the number of inversion iterations is 12 times. Figures 7(a) and 7(b) show the objective function fitting and the root mean square (RMS) error during the inversion process, respectively. It can be seen from the figures that the data fitting is poor and the objective function decreases steadily, indicating that the L_BFGS in this paper has good convergence for the three-dimensional borehole-surface resistivity method. Figures 8(a) and 8(b) show the inversion result profiles of XOZ and YOZ, respectively. It can be seen that the inversion result of the synthetic model data is still in good agreement with the real model in the presence of noise, and the location of the underground low-resistance anomaly is the same as the resistivity value, which verifies the effectiveness of the inversion method proposed in this paper.

4.2. Inversion of Buried Cuboid Model under Valley.

The model of the buried anomaly under the valley is shown in Figure 9. The lowest part of the valley is 10 m above the ground, and the entire depression is symmetrical about the minimum. The horizontal span is 45 m . The resistivities of the background half-space and the low-resistance body are $\rho_0 = 100 \Omega\text{m}$ and $\rho_1 = 10 \Omega\text{m}$, respectively. The size of the low-resistance cuboid is $10 \text{ m} \times 10 \text{ m} \times 5 \text{ m}$. The buried depths of the cuboid from the top to the ground and from the bottom to the ground are $h = 5 \text{ m}$ and 10 m , and the horizontal distance between the anomalous body and the drilling on both sides is $d = 5 \text{ m}$. The blue triangles represent the locations of the two well-heads $(40, 50, -8)$ and $(60, 50, -8)$. The red five-pointed star represents the origin of the Cartesian coordinate system $(50, 50, 0)$. There are a total of 5 survey lines in the survey area in inversion. The distance between survey lines is 5 m . The number of measuring points selected in each survey line is 79. The position coordinates of measuring point M (measuring electrode) along the X direction are $x = 11 \sim 89 \text{ m}$ and $y = 40 \sim 60 \text{ m}$ with an interval of 1 m . The total measuring points are 395. The range of the source point A (source electrode) is from -5 m to -25 m downhole, with an interval of 5 m . Figure 10 shows the unstructured tetrahedral meshes used in the forwarding and inversion of the model. In order to improve the accuracy of the forward modeling and reduce the numerical simulation error near the source point, the forward meshes are refined in the vicinity of the survey point, the source point, and the anomalous body. The inversion mesh is at the source point. The total number of tetrahedral cells is 1247660. Encrypted

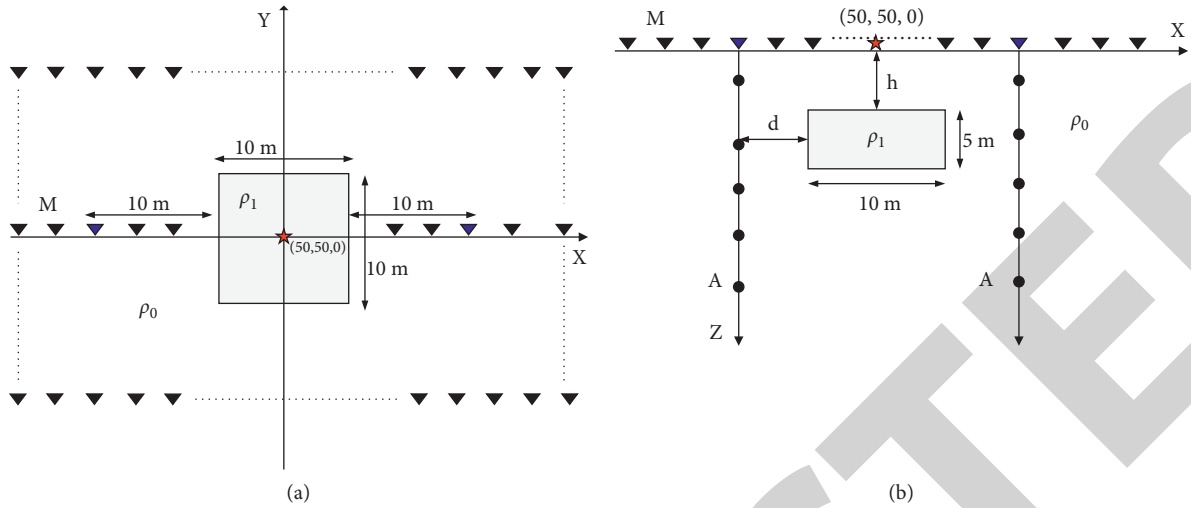


FIGURE 5: Geometrical model of a flat surface with a cube. (a) XOY plane view of the model; (b) XOZ cross-sectional view of the model.

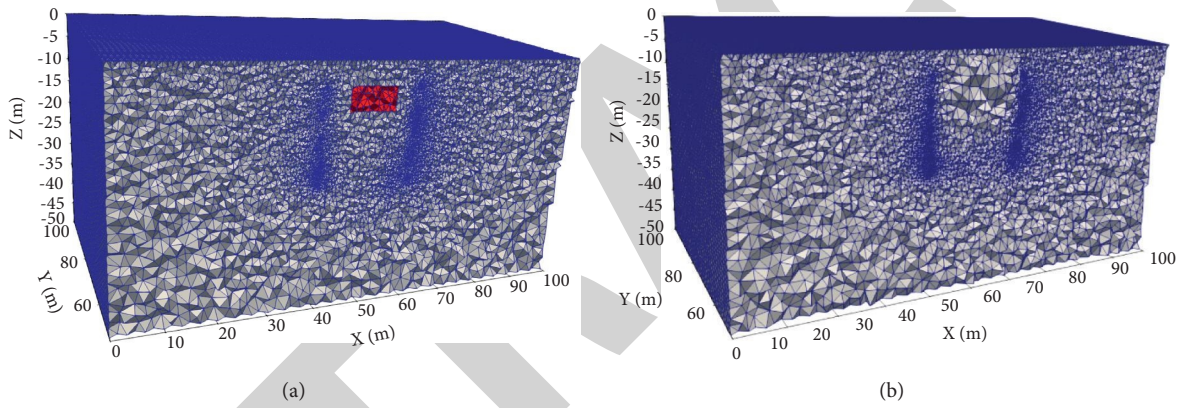


FIGURE 6: Forward and inversion grid of the buried rectangular model under the flat surface. (a) Forward mesh and (b) inversion mesh.

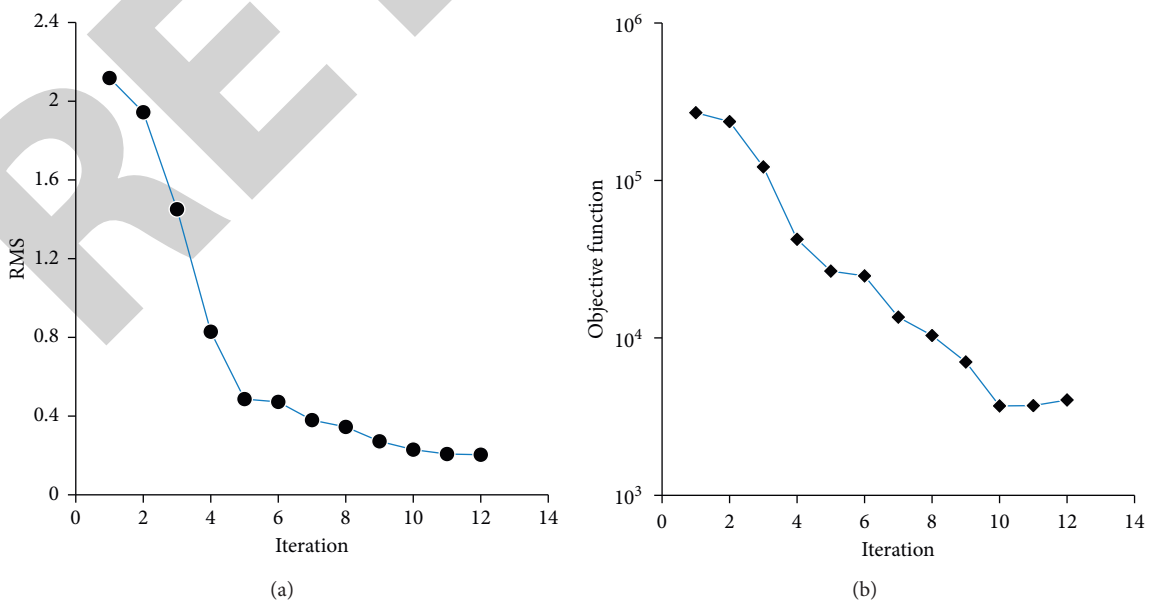


FIGURE 7: The relationship between inversion parameters and the number of iterations. (a) Data relative fit difference RMS; (b) fitting of objective function.

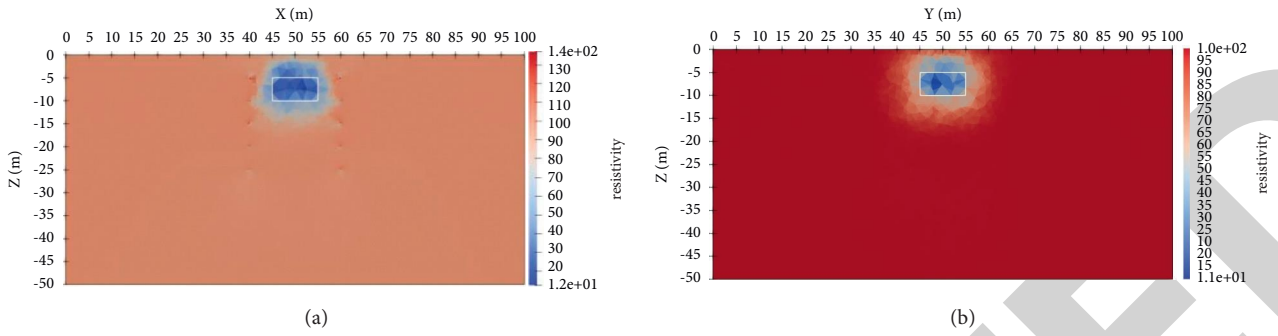


FIGURE 8: Inversion results of anomalous bodies under the flat surface. (a) Slice of resistivity inversion result at XOZ profile; (b) slice of resistivity inversion result at YOZ profile. The outline of the true model is indicated by the white rectangles.

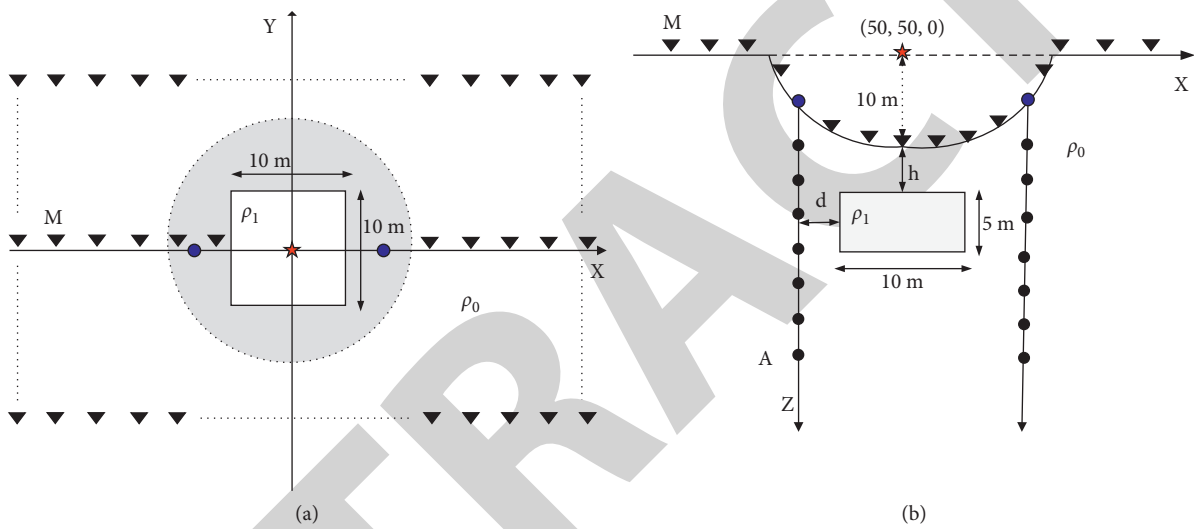


FIGURE 9: The geometry of valley topographical model with a cube. (a) XOY plane view; (b) XOZ cross-sectional view.

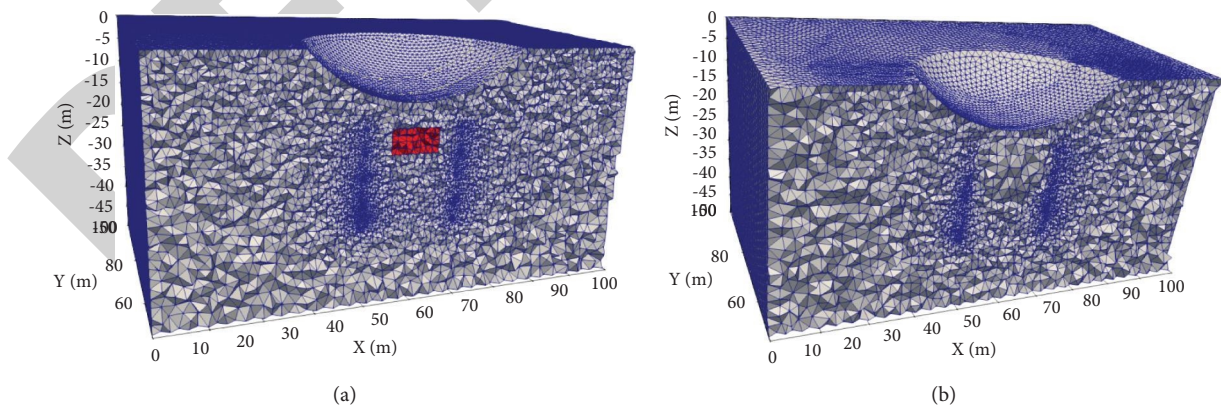


FIGURE 10: Forward and inversion grid of buried rectangular model under valley topography. (a) Forward mesh; (b) inversion mesh.

with the measuring point, the total number of inversion grid tetrahedral cells is 1169531. The selection of the inversion parameters is consistent with the inversion model under a flat surface. The number of inversion iterations is 17 times. The relative fitting error RMS of the data during the inversion

process is shown in Figure 11(a). It can be seen from the figure that the data fitting is poor. The steady decline indicates that the L_BFGS inversion method has good convergence in this paper. Figure 11(b) shows the slice of resistivity 3D inversion result, while Figures 11(c) and 11(d) show the results of slices

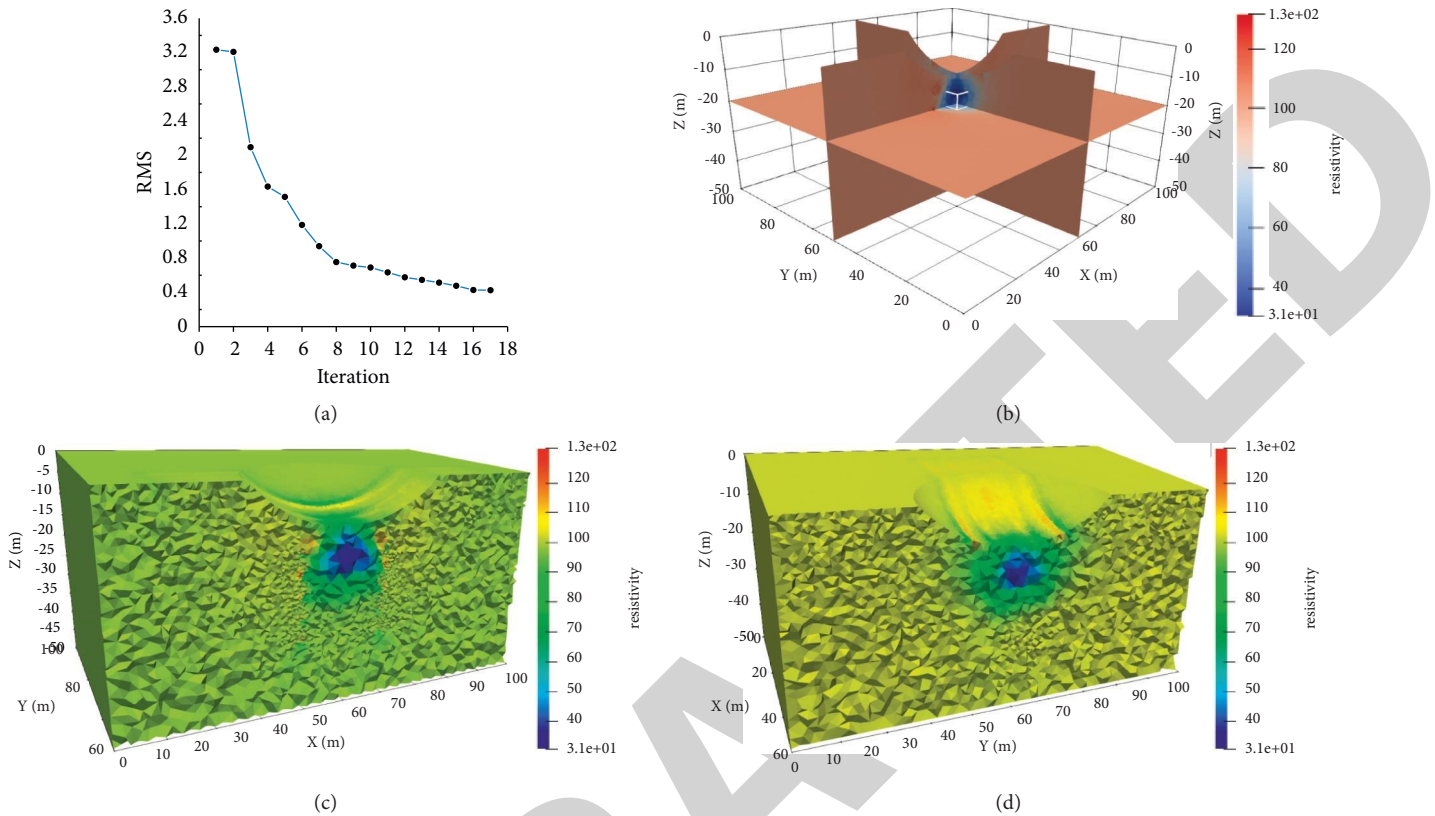


FIGURE 11: Inversion results of anomalous bodies under valley topographical model. (a) The relative fitting error RMS during the inversion process; (b) slice of resistivity 3D inversion result; (c) slice of resistivity inversion result at XOZ profile; (d) slice of resistivity inversion result at YOZ profile. The outline of the true model is indicated by the white boxes.

at XOZ and YOZ profiles, respectively, under valley topography. The topography effects can be seen in the figures. Under the circumstances, the inversion result of the synthetic model data is in good agreement with the real model, and the location of the underground low-resistance anomaly is the same as the resistivity value, which effectively eliminates the influence of topography and verifies the effectiveness of the proposed inversion method.

4.3. Inversion of the Buried Cuboid Model under Mountain.

The buried rectangular model under the mountain is shown in Figure 12. The highest part of the mountain relative to the ground is 10 m high, the entire uplift is symmetrical about the maximum, and the horizontal span is 45 m. The resistivities of the background half-space and the low-resistance body are $\rho_0 = 100 \Omega\text{m}$ and $\rho_1 = 10 \Omega\text{m}$, respectively. The size of the low-resistance rectangular block is $10 \text{ m} \times 10 \text{ m} \times 5 \text{ m}$. The buried depths of the cuboid from the top to the ground and from the bottom to the ground are $h = 5 \text{ m}$ and 10 m , respectively. The horizontal distance between the abnormal body and the drilling on both sides is $d = 5 \text{ m}$. The blue triangles represent the locations of the two wellheads (40, 50, 8) and (60, 50, 8). The red five-pointed star represents the origin of the Cartesian coordinate system (50, 50, 0). There are a total of 5 survey lines in the survey area of inversion. The survey lines are laid on the ground. The measuring

device is placed along the positive direction of the x -axis with 99 measuring electrodes separated by 1 m to pass through the top of the mountain. The distance between the survey lines is 5 m. The position coordinates of measuring point M (measuring electrode) are $x = 1 \sim 99 \text{ m}$ and $y = 40 \sim 60 \text{ m}$, and the total number of measuring points is 495. The range of the source point A (source electrode) is from -5 m to -25 m downhole, with an interval of 5 m. Figure 13 shows the unstructured tetrahedral meshes used in the forwarding and inversion of the model. In order to improve the accuracy of the forward modeling and reduce the numerical simulation error near the source point, the forward meshes are refined in the vicinity of the measuring point, the source point, and the anomalous body. The total number of tetrahedral cells is 1105427. The inversion mesh is refined at the source and the measuring points. The total number of tetrahedral cells is 732012. The selection of inversion parameters is consistent with the inversion model under a flat surface. The number of inversion iterations is 9 times. The RMS change during the inversion process is shown in Figure 14(a). It can be seen from the figure that the relative RMS of the data is poorly fitted. The steady decline of RMS indicates that the L_BFGS inversion method in this paper has good convergence. Figure 14(b) shows the slice of resistivity 3D inversion result, while Figures 14(c) and 14(d) show the results slices at XOZ and YOZ profiles, respectively, under mountain topography. It can be seen from the figures that the inversion result of the

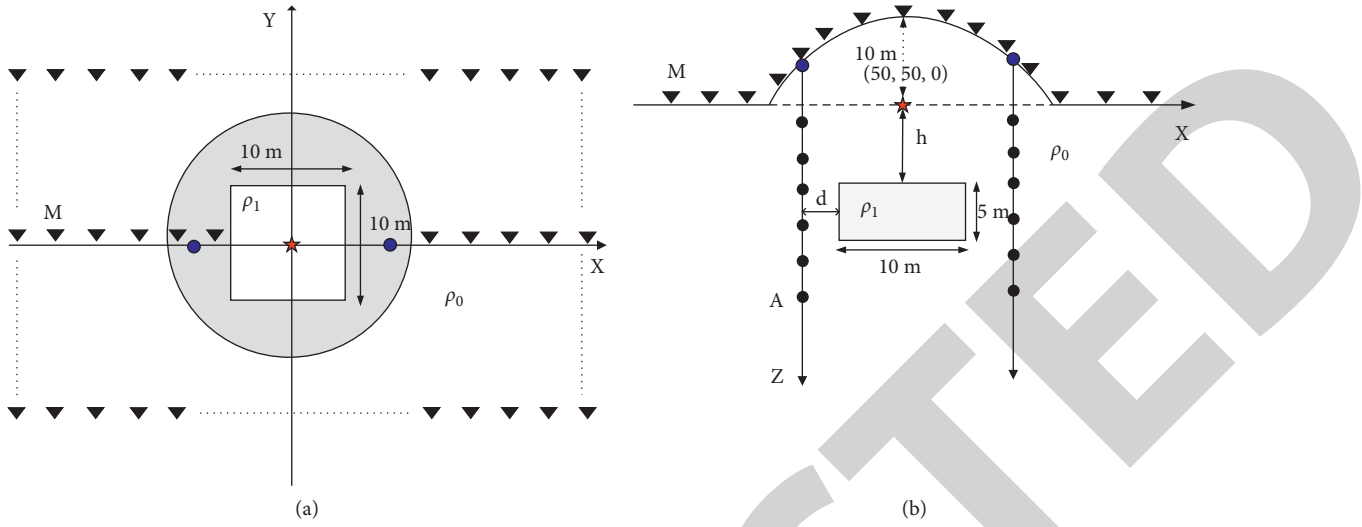


FIGURE 12: The geometry of mountain topographical model with a cube. (a) XOY plane view; (b) XOZ cross-sectional view.

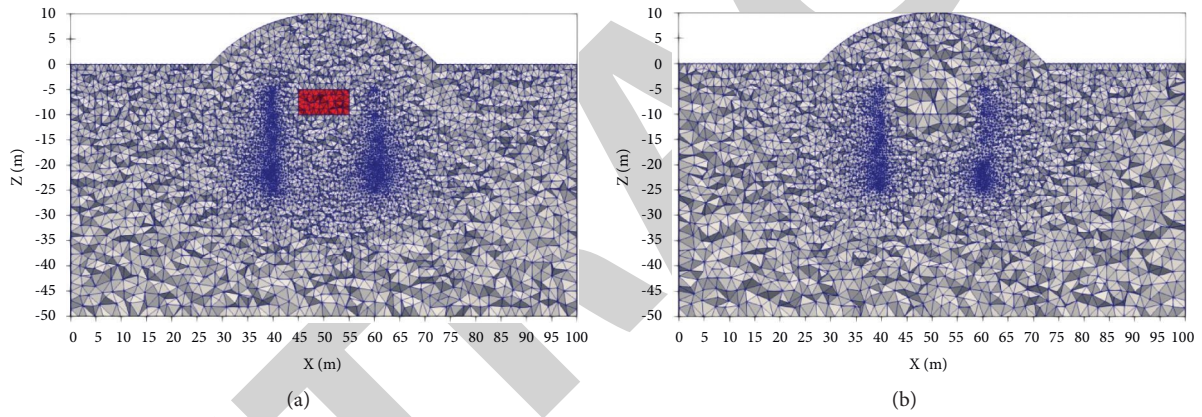


FIGURE 13: Forward and inversion grid of buried rectangular model under mountain topography. (a) Forward mesh; (b) inversion mesh.

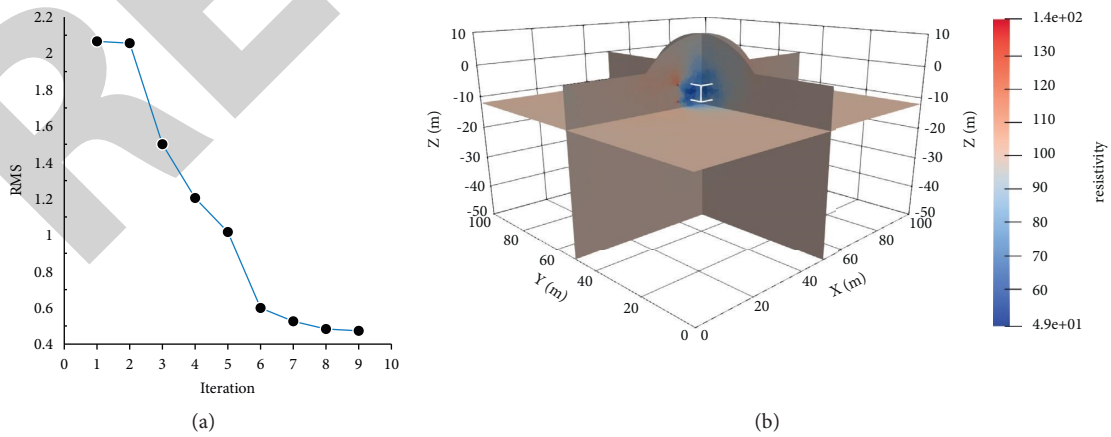


FIGURE 14: Continued.

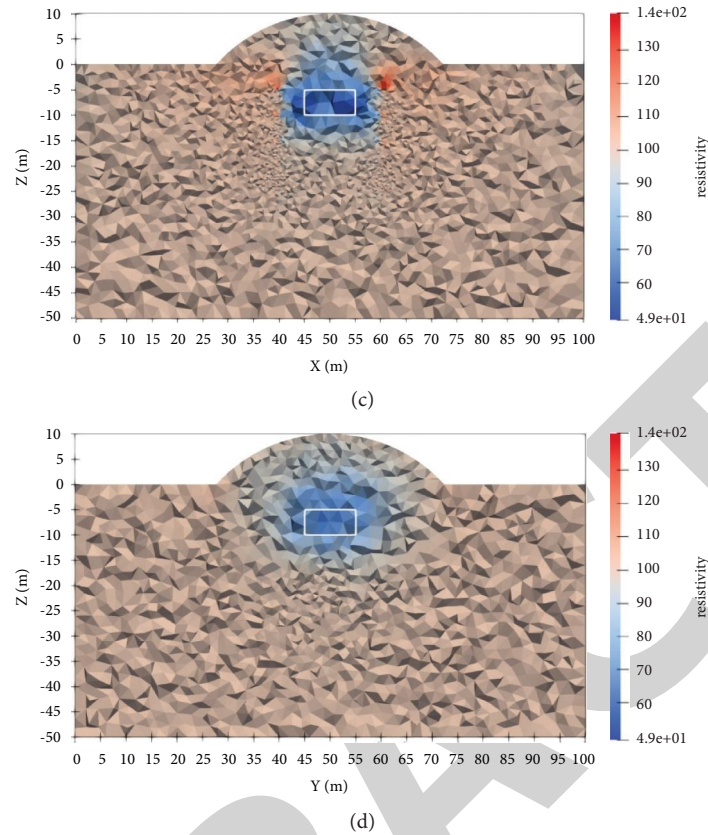


FIGURE 14: Inversion results of anomalous bodies under mountain topographical model. (a) The change in the relative RMS during the inversion process; (b) slice of resistivity 3D inversion result; (c) slice of resistivity inversion result at XOZ profile; (d) slice of resistivity inversion result at YOZ profile. The outline of the true model is indicated by the white rectangles.

synthetic model data is in good agreement with the real model. The location of the underground low-resistance anomaly is the same as the resistivity value, which effectively eliminates the influence of topography and verifies the effectiveness of the inversion method proposed in this paper.

5. Conclusion

This paper successfully realizes and develops the three-dimensional inversion of the borehole-to-surface resistivity method in nonflat surface topography based on the unstructured finite element method and the limited memory L_BFGS method. In order to verify the effectiveness of the proposed algorithm, numerical simulations of inversion of synthetic data for flat, valley, and mountain topographies are conducted. The obtained results validate that the proposed algorithm has high stability, and the inversion results better restore the distribution characteristics of low-resistance anomalies under various topography conditions. Future research will focus on utilizing the algorithm proposed in this paper to carry out the inversion of field-data applications resistivity. A reasonable application of a variety of information constraints can improve the accuracy of the position and shape of anomalies in the imaging results. Future research plan also includes the use of regularization and related techniques to achieve high-precision underground imaging with prior information.

Data Availability

No data were used to support this paper.

Conflicts of Interest

The authors declare that they have no conflicts of interest.

References

- [1] J. X. Liu, R. Zhao, and Z. W. Guo, "Research progress of electromagnetic methods in the exploration of metal deposits," *Progress in Geophysics*, vol. 34, pp. 151–160, 2019.
- [2] Q. T. Lv, X. P. Zhang, J. T. Tang et al., "Review on advancement in technology and equipment of geophysical exploration for metallic deposits in China," *Chinese Journal of Geophysics*, vol. 62, pp. 3629–3664, 2019.
- [3] X. Wang, M. Huang, and L. Wan, "Joint 2D-DOD and 2D-DOA estimation for coprime EMVS-MIMO radar," *Circuits, Systems, and Signal Processing*, vol. 40, no. 6, pp. 2950–2966, 2021.
- [4] J. He, L. Li, and T. Shu, "Sparse nested arrays with spatially spread orthogonal dipoles: high accuracy passive direction finding with less mutual coupling," *IEEE Transactions on Aerospace and Electronic Systems*, vol. 57, no. 4, pp. 2337–2345, 2021.
- [5] F. Wen, J. Shi, and Z. Zhang, "Closed-form estimation algorithm for EMVS-MIMO radar with arbitrary sensor geometry," *Signal Processing*, vol. 186, pp. 108–117, 2021.

- [6] H. Wang, X. Li, R. H. Jhaveri et al., "Sparse Bayesian learning based channel estimation in FBMC/OQAM industrial IoT networks," *Computer Communications*, vol. 176, pp. 40–45, 2021.
- [7] J. Shi, F. Wen, and T. Liu, "Nested MIMO radar: coarrays, tensor modeling and angle estimation," *IEEE Transactions on Aerospace and Electronic Systems*, vol. 57, pp. 573–585, 2020.
- [8] H. Wang, L. Xu, Z. Yan, and T. A. Gulliver, "Low-complexity MIMO-FBMC sparse channel parameter estimation for industrial big data communications," *IEEE Transactions on Industrial Informatics*, vol. 17, no. 5, pp. 3422–3430, 2021.
- [9] L. Wan, K. Liu, Y. C. Liang, and Z. Tong, "DOA and polarization estimation for non-circular signals in 3-D millimeter wave polarized massive MIMO systems," *IEEE Wireless Communications*, vol. 20, pp. 3152–3167, 2017.
- [10] X. P. Wu, Y. Liu, and W. Wang, "3D resistivity inversion incorporating topography based on unstructured meshes," *Chinese Journal of Geophysics*, vol. 58, pp. 2706–2717, 2015.
- [11] Z. Wang, A. P. Wu, and G. Li, "Forward modeling of borehole-ground induced polarization method under undulating topography," *Geophysical Prospecting for Petroleum*, vol. 57, no. 6, pp. 927–935, 2018.
- [12] J. T. Tang, J. F. Zhang, B. Feng, J.-Y. Lin, and C.-S. Liu, "Determination of borders for resistive oil and gas reservoirs by deviation rate using the hole-to-surface resistivity method," *Chinese Journal of Geophysics*, vol. 50, pp. 926–931, 2007.
- [13] Y. Li and K. Spitzer, "Finite element resistivity modelling for three-dimensional structures with arbitrary anisotropy," *Physics of the Earth and Planetary Interiors*, vol. 150, no. 1–3, pp. 15–27, 2005.
- [14] X. Wu, "A 3-D finite-element algorithm for DC resistivity modelling using the shifted incomplete Cholesky conjugate gradient method," *Geophysical Journal International*, vol. 154, no. 3, pp. 947–956, 2003.
- [15] X. P. Wu and T. T. Wang, "A 3-D finite-element resistivity forward modeling using conjugate gradient algorithm," *Chinese Journal of Geophysics*, vol. 46, pp. 428–432, 2003.
- [16] Y. Li and K. Spitzer, "Three-dimensional DC resistivity forward modelling using finite elements in comparison with finite-difference solutions," *Geophysical Journal International*, vol. 151, no. 3, pp. 924–934, 2002.
- [17] M. Blome, H. R. Maurer, and K. Schmidt, "Advances in three-dimensional geoelectric forward solver techniques," *Geophysical Journal International*, vol. 176, no. 3, pp. 740–752, 2009.
- [18] T. Günther, C. Rücker, and K. Spitzer, "Three-dimensional modelling and inversion of dc resistivity data incorporating topography - II. Inversion," *Geophysical Journal International*, vol. 166, no. 2, pp. 506–517, 2006.
- [19] C. Rücker, T. Günther, and K. Spitzer, "Three-dimensional modelling and inversion of dc resistivity data incorporating topography-I Modelling," *Geophysical Journal International*, vol. 166, no. 2, pp. 495–505, 2006.
- [20] Z. Ren and J. Tang, "3D direct current resistivity modeling with unstructured mesh by adaptive finite-element method," *Geophysics*, vol. 75, no. 1, pp. H7–H17, 2010.
- [21] Z. Ren and J. Tang, "A goal-oriented adaptive finite-element approach for multi-electrode resistivity system," *Geophysical Journal International*, vol. 199, no. 1, pp. 136–145, 2014.
- [22] Z. Ren, L. Qiu, J. Tang, X. Wu, X. Xiao, and Z. Zhou, "3-D direct current resistivity anisotropic modelling by goal-oriented adaptive finite element methods," *Geophysical Journal International*, vol. 212, no. 1, pp. 76–87, 2018.
- [23] Y. Sasaki, "3-D resistivity inversion using the finite-element method," *Geophysics*, vol. 59, no. 12, pp. 1839–1848, 1994.
- [24] W. Wang, X. Wu, and K. Spitzer, "Three-dimensional DC anisotropic resistivity modelling using finite elements on unstructured grids," *Geophysical Journal International*, vol. 193, no. 2, pp. 734–746, 2013.
- [25] B. Zhou and S. A. Greenhalgh, "Finite element three dimensional direct current resistivity modelling: accuracy and efficiency considerations," *Geophysical Journal International*, vol. 145, pp. 679–688, 2001.
- [26] J. Zhang, R. L. Mackie, and T. R. Madden, "3-D resistivity forward modeling and inversion using conjugate gradients," *Geophysics*, vol. 60, no. 5, pp. 1313–1325, 1995.
- [27] K. Spitzer, "A 3-D finite-difference algorithm for DC resistivity modelling using conjugate gradient methods," *Geophysical Journal International*, vol. 123, no. 3, pp. 903–914, 1995.
- [28] X. Wu, Y. Xiao, C. Qi, and T. Wang, "Computations of secondary potential for 3D DC resistivity modelling using an incomplete Choleski conjugate-gradient method," *Geophysical Prospecting*, vol. 51, no. 6, pp. 567–577, 2003.
- [29] S. Zhao and M. J. Yedlin, "Some refinements on the finite-difference method for 3-D dc resistivity modeling," *Geophysics*, vol. 61, no. 5, pp. 1301–1307, 1996.
- [30] X. P. Wu, G. M. Xu, and S. C. Li, "The calculation of three-dimensional geoelectric field of point source by incomplete cholesky conjugate gradient method," *Chinese Journal of Geophysics*, vol. 41, pp. 848–855, 1998.
- [31] J. T. Tang, F. Y. Wang, and Z. Y. Ren, "2.5 D resistivity modeling by adaptive finite-element method with unstructured triangulation," *Chinese Journal of Geophysics*, vol. 53, pp. 708–716, 2010.
- [32] Z. Y. Ren and J. T. Tang, "Finite element modeling of 3-D DC resistivity using locally refined unstructured meshes," *Chinese Journal of Geophysics*, vol. 52, pp. 2627–2634, 2009.
- [33] N. Y. Gundogdu and M. E. Candansayar, "Three-dimensional regularized inversion of DC resistivity data with different stabilizing functionals," *Geophysics*, vol. 83, pp. E399–E407, 2018.
- [34] L. G. Guo, G. L. Dai, and B. C. Yang, "3D resistivity inversion with multiple priori-information constraint," *Oil Geophysical Prospecting*, vol. 53, pp. 1333–1340, 2018.
- [35] R. H. Peng, X. Y. Hu, and B. Han, "3D inversion of frequency-domain CSEM data based on Gauss-Newton optimization," *Chinese Journal of Geophysics*, vol. 59, pp. 3470–3481, 2016.
- [36] D. W. Oldenburg, E. Haber, and R. Shekhtman, "Three dimensional inversion of multisource time domain electromagnetic data," *Geophysics*, vol. 78, no. 1, pp. E47–E57, 2013.
- [37] A. Pidlisecky, E. Haber, and R. Knight, "RESINVM3D: a 3D resistivity inversion package," *Geophysics*, vol. 72, no. 2, pp. H1–H10, 2007.
- [38] X. Cao, X. Huang, C. Yin, L. Yan, and B. Zhang, "3D MT anisotropic inversion based on unstructured finite-element method," *Journal of Environmental & Engineering Geophysics*, vol. 26, pp. 46–60, 2021.
- [39] Z. J. Hui, C. C. Yin, Y. H. Liu, B. Zhang, X. Y. Ren, and C. Wang, "3D inversion of time-domain marine EM data based on unstructured finite-element method," *Chinese Journal of Geophysics*, vol. 63, pp. 3167–3179, 2020.
- [40] H. Yu, J. Z. Deng, H. Chen et al., "Three-dimensional magnetotelluric inversion under topographic relief based on the limited-memory quasi-Newton algorithm(L_BFGS)," *Chinese Journal of Geophysics*, vol. 62, pp. 3175–3188, 2019.

- [41] Y. H. Liu and C. C. Yin, "3D inversion for frequency-domain HEM data," *Chinese Journal of Geophysics*, vol. 56, pp. 4278–4287, 2013.
- [42] E. Haber, D. W. Oldenburg, and R. Shekhtman, "Inversion of time domain three-dimensional electromagnetic data," *Geophysical Journal International*, vol. 171, no. 2, pp. 550–564, 2007.
- [43] D. Avdeev and A. Avdeeva, "3D Magnetotelluric inversion using a limited-memory quasi-Newton optimization," *Geophysics*, vol. 74, no. 3, pp. F45–F57, 2009.
- [44] Y. Xiao, Z. Wei, and Z. Wang, "A limited memory BFGS-type method for large-scale unconstrained optimization," *Computers & Mathematics with Applications*, vol. 56, no. 4, pp. 1001–1009, 2008.
- [45] A. Avdeeva and D. Avdeev, "A limited-memory quasi-Newton inversion for 1D magnetotellurics," *Geophysics*, vol. 71, no. 5, pp. G191–G196, 2006.
- [46] E. Haber, "Quasi-Newton methods for large-scale electromagnetic inverse problems," *Inverse Problems*, vol. 21, no. 1, pp. 305–323, 2005.
- [47] G. A. Newman and P. T. Boggs, "Solution accelerators for large-scale three-dimensional electromagnetic inverse problems," *Inverse Problems*, vol. 20, no. 6, pp. S151–S170, 2004.
- [48] S. G. Nash and J. Nocedal, "A numerical study of the limited memory BFGS method and the truncated-Newton method for large scale optimization," *SIAM Journal on Optimization*, vol. 1, no. 3, pp. 358–372, 1991.
- [49] D. C. Liu and J. Nocedal, "On the limited memory BFGS method for large scale optimization," *Mathematical Programming*, vol. 45, no. 1-3, pp. 503–528, 1989.
- [50] J. Nocedal, "Updating quasi-Newton matrices with limited storage," *Mathematics of Computation*, vol. 35, no. 151, 773 pages, 1980.
- [51] H. Ma, Y. Guo, P. P. Wu, and T. Hamimah, "3-D joint inversion of multi-array data set in the resistivity method based on MPI parallel algorithm," *Chinese Journal of Geophysics*, vol. 61, pp. 5052–5065, 2018.
- [52] W. Rodi and R. L. Mackie, "Nonlinear conjugate gradients algorithm for 2-D magnetotelluric inversion," *Geophysics*, vol. 66, no. 1, pp. 174–187, 2001.
- [53] G. A. Newman and D. L. Alumbaugh, "Three-dimensional magnetotelluric inversion using non-linear conjugate gradients," *Geophysical Journal International*, vol. 140, no. 2, pp. 410–424, 2000.
- [54] X. P. Wu and G. M. Xu, "Study on 3-D resistivity inversion using conjugate method," *Chinese Journal of Geophysics*, vol. 43, pp. 420–427, 2000.
- [55] S. Z. Xu, *Finite Element Method in Geophysics*, Science Press, Beijing, China, 1994.
- [56] C. Geuzaine and J.-F. Remacle, "Gmsh: a 3-D finite element mesh generator with built-in pre- and post-processing facilities," *International Journal for Numerical Methods in Engineering*, vol. 79, no. 11, pp. 1309–1331, 2009.
- [57] J. Ahrens, B. Geveci, and C. Law, "ParaView: an end-user tool for large data visualization," *Visualization Handbook*, Elsevier, Amsterdam, The Netherlands, 2005.
- [58] K. L. Cook and R. G. Van Nostrand, "Interpretation of resistivity data over filled sinks," *Geophysics*, vol. 19, no. 4, pp. 761–790, 1954.
- [59] J. Nocedal and S. J. Wright, *Numerical Optimization*, Springer-Verlag, New York, NY, USA, 1999.